remote sensing

MDPI

Article

Hydrological Cycle in the Arabian Sea Region from GRACE/GRACE-FO Missions and ERA5 Data

Ahmed Kamel Boulahia [1], David García-García [1,*], Mario Trottini [2], Juan-Manuel Sayol [1] and M. Isabel Vigo [1]

[1] Applied Mathematics Department, University of Alicante, 03690 Alicante, Spain; bak2@gcloud.ua.es (A.K.B.); juanma.sayol@ua.es (J.-M.S.); vigo@ua.es (M.I.V.)
[2] Mathematics Department, University of Alicante, 03690 Alicante, Spain; mario.trottini@ua.es
* Correspondence: d.garcia@ua.es

Abstract: The Arabian Gulf, a semi-enclosed basin in the Middle East, connects to the Indian Ocean through the Strait of Hormuz and is surrounded by seven arid countries. This study examines the water cycle of the Gulf and its surrounding areas using data from the GRACE and GRACE Follow-On missions, along with ERA5 atmospheric reanalysis data, from 05/2002 to 05/2017 and from 07/2018 to 12/2023. Our findings reveal a persistent water deficit due to high evaporation rates, averaging 370 $\pm$ 3 km^3/year, greatly surpassing precipitation, which accounts for only 15% of the evaporative loss. Continental runoff provides one-fifth of the needed water, while the remaining deficit, approximately 274 $\pm$ 10 km^3/year, is balanced by net inflow of saltwater from the Indian Ocean. Seasonal variations show the lowest net inflow of 26 $\pm$ 49 km^3/year in March and the highest of 586 $\pm$ 53 km^3/year in November, driven by net evaporation, continental input, and changes in the Gulf's water budget. This study highlights the complex hydrological dynamics influenced by climate patterns and provides a baseline for future research in the region, which will be needed to quantify the expected changes in the hydrological cycle due to climate change.

Keywords: Arabian Gulf; water transport components; Strait of Hormuz; runoff; net water inflow

Citation: Boulahia, A.K.; García-García, D.; Trottini, M.; Sayol, J.-M.; Vigo, M.I. Hydrological Cycle in the Arabian Sea Region from GRACE/GRACE-FO Missions and ERA5 Data. *Remote Sens.* **2024**, *16*, 3577. https://doi.org/10.3390/rs16193577

Academic Editor: Liming He

Received: 5 August 2024
Revised: 20 September 2024
Accepted: 22 September 2024
Published: 25 September 2024

1. Introduction

The Persian, or Arabian, Gulf is a semi-enclosed sea located in the Middle East, between latitudes 24°N and 31°N and longitudes 48°E and 56°E, and bordered in counterclockwise order starting from the east by Iran, Iraq, Kuwait, Saudi Arabia, Bahrain, Qatar, and the United Arab Emirates (Figure 1). The Gulf is shallow, with average and maximum depths of 50 m and 110 m, respectively, and covers an area of approximately 2.5 $\times$ 10^5 km^2. It is about 1000 km long and varies in width from 56 km at the Strait of Hormuz to a maximum of 340 km [1]. The Arabian Gulf is connected to the Gulf of Oman through the Strait of Hormuz, and then to the Arabian Sea in the northern Indian Ocean (Figure 1).

The Strait of Hormuz is one of the most crowded waterways because it is the only access point to some of the largest oil-producing countries in the world, such as Saudi Arabia, Iran, the United Arab Emirates, and Iraq. These countries produce about 20% of all the oil traded globally, which is exported by sea to other parts of the planet, generating a lot of maritime traffic in the Strait of Hormuz. In fact, around 40% of the world's oil transported by ship passes through this narrow passage [2]. The high volume of shipping and bottom trawling in the region makes in situ oceanographic data collections extremely difficult, as instruments could be damaged by ships or fishing gear [2]. In this context, remote sensing techniques are crucial to study the net transport of water through the Strait of Hormuz.

The hydrological cycle, also known as the water cycle, is the continuous movement of water between and within the atmosphere, the continents, and the oceans, which plays a crucial role in the regulation of weather patterns and in determining the availability of freshwater, which is essential for the life of humans and ecosystems. The continental

region surrounding the Arabian Gulf is characterized by an arid climate and limited water resources. While the underground water resources are substantial, their saline concentration is extremely high, necessitating desalination for human activities. In fact, rapid population growth, particularly in urban areas, is leading to an increase in water demand and, therefore, desalination. During the desalinization process, salt and minerals are removed from sea or brackish water through several processes. This disrupts the natural water cycle by altering the balance of salt and freshwater in the environment. In addition, the intake of sea/brackish water and the discharge of brine water during the desalination process can also affect the local marine environment. The intake of large amounts of seawater can trap and kill marine life, while the discharge of brine can raise the salinity levels of nearby seawater and affect the ecosystem [3]. The Arabian Gulf countries have a cumulative desalination capacity of around 11×10^6 m^3/day, which is about 45% of the global desalination activity [3]. Understanding the hydrological dynamics of the Arabian Gulf is important due to the various environmental factors that impact it, especially the exchanges with the open ocean.

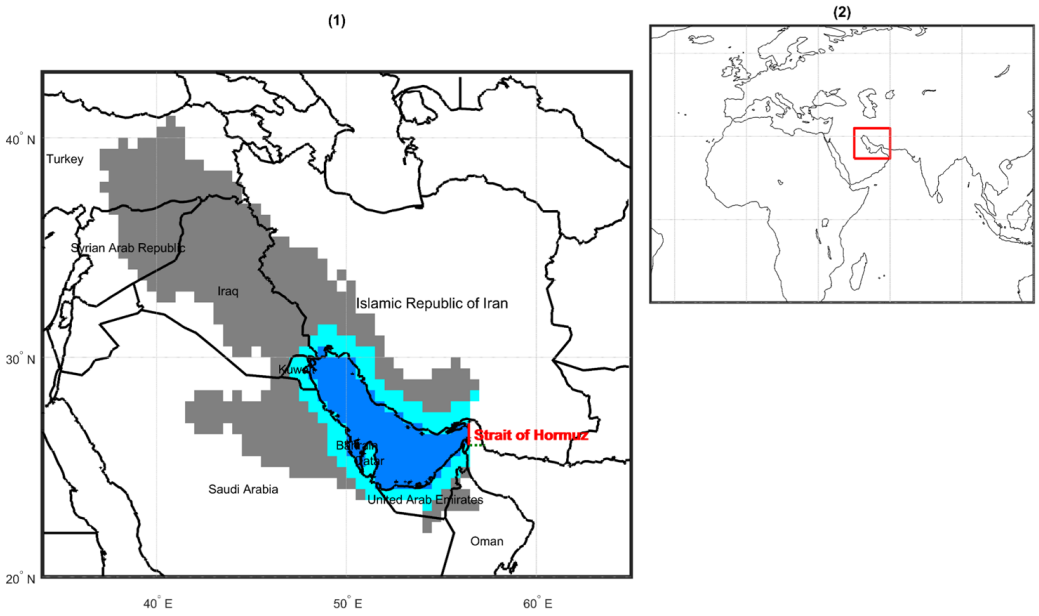

Figure 1. (**1**) Arabian Gulf (blue region) and continental region draining into the Gulf (gray region), as defined by the Global Continental Runoff Routing Framework (Oki and Sud, 1998) [4]. Missing points between them (cyan region) are suppressed in this study to reduce leakage signals in GRACE data. An added subplot (**2**) shows the geographical location of the study region in the world.

In the sea, the Arabian Gulf receives freshwater from riverine inflow and precipitation (P), but a larger water budget is lost via evaporation (E), producing a deficit of water that must be restored by importing seawater from the Gulf of Oman. This loss of freshwater makes the Arabian Gulf a hypersaline basin with an inverse estuarine circulation, where less saline and warmer water from the Indian Ocean enters the Arabian Gulf near the surface, and denser (colder and saltier) water moves in the opposite direction in the deeper layers [5]. This density difference explains why the Arabian Gulf circulation is typically modeled with two isopycnal levels. The salty water masses leaving the Arabian Gulf spread out in the Gulf of Oman, and some pathways can reach the Atlantic Ocean [6] and the Bay of Bengal [7]. The upper outflowing water mixes because of changes in temperature via diffusive convection, and the deeper one mixes via salt fingering [8]. The Arabian Gulf's climatological conditions, circulation variability, and water exchange through the Strait of Hormuz have been studied through modeling and in situ observational research over the past few decades [9,10]. However, there has been a serious lack of in situ measurements in the last 25 years, since most of the latest studies are based on measurement campaigns from

the period 1996–1998 [11]. Remote sensing measurements can partially compensate for the lack of in situ measurements. In this study, we will examine such remote measurements to better understand the current hydrological cycle in the region.

Understanding the hydrological cycle is essential to effectively manage freshwater resources and sustain human and natural life. It is important to monitor the water cycle to obtain benchmarks to quantify the impact of climate change in the future, as it is expected to affect the hydrological cycle, intensifying the latter at a global level [12–17]. Because each region responds differently to changes in the hydrological cycle, it is critical to monitor water cycles and their temporal evolution regionally. In this study, we investigate the hydrological cycle of the Arabian Gulf and the continental catchments that drain into it. In particular, in a first phase, we will study the P, E, and variation in continental water reserves to infer the water contribution of the continents to the Arabian Gulf. We will then repeat the analysis at sea to study the net water exchange between the Gulf and the Indian Ocean. To do this, we will use the time-variable gravity observations performed by the Gravity Recovery and Climate Experiment (GRACE) and GRACE Follow-On satellites, and P and E from ERA5 atmospheric reanalysis data for the period 2002–2023. Section 2 describes the methodology, which has been successfully applied at the ocean global scale [18], in the Mediterranean–Black Sea system [19], and in the Baltic Sea [20]. Data are also detailed in Section 2. Section 3 presents the average, seasonal, and non-seasonal signal of all the water transport (WT) components. It also analyzes their connections to climate indices. Finally, Section 4 discusses the results and presents the conclusions.

2. Methods and Data

2.1. Methods

The Arabian Gulf and the surrounding continental catchments region exchange freshwater with the atmosphere through P and E processes. Positive (negative) net precipitation, $P-E$, increases (decreases) the water budget (W), producing variations in W, hereafter dW. In the continents, when P exceeds E, the water not stored flows into the sea (R) through three mechanisms: river runoff, surface runoff outside the course of rivers, and submarine groundwater discharge. Then, the general hydrological budget equation can be written as [21]:

$$dW = P - E - R, \text{ for land.} \quad (1)$$

In the ocean, the Arabian Gulf receives R from land and has a net water exchange (N) with the Oman Sea through the Strait of Hormuz. Therefore, the hydrological budget equation can be written as:

$$dW = P - E + R + N, \text{ for ocean.} \quad (2)$$

Positive and negative values of N indicate water inflow to and outflow from the Arabian Gulf, respectively.

The ocean water flux, N, will be estimated in a two-step process following the approach in [18]. First, knowing P, E, and dW in the continental catchment region draining to the Arabian Gulf, the corresponding R can be estimated as a residual in Equation (1). Second, knowing P, E, dW, and R (estimated in the previous step) in the Arabian Gulf, the corresponding N can be estimated as a residual in Equation (2).

If P, E, and dW are available at a monthly frequency, then monthly time series of R and N can be estimated. For each time series, the following harmonic regression model, with a linear trend, and annual and semi-annual components will be considered:

$$C_t = p_0 + p_1.t + A_a\cos(\omega_a.t - \varphi_a) + A_{sa}\cos(\omega_{sa}.t - \varphi_{sa}), \quad (3)$$

where t represents time, C_t denotes the value of the target time series at a given time t, (ω, A, φ) = (frequency, amplitude, phase), and the suffixes a and sa refer to annual and semi-annual terms. Note that φ_a (in degrees) indicates the day of the year on which the

annual maximum occurs, with one degree roughly corresponding to one day. Using the cosine angle subtraction formula, the equation can be transformed into a linear regression model with independent variables: $\cos(\omega_a \cdot t)$, $\sin(\omega_a \cdot t)$, $\cos(\omega_{sa} \cdot t)$, and $\sin(\omega_{sa} \cdot t)$ [20].

The standard deviations (SDs) and 95% confidence intervals (CIs) for the mean values, trends, and seasonal signals of the components, as well as correlations reported in Sections 3.1–3.3, have been evaluated using the stationary bootstrap scheme in [22], with the optimal block length selected according to [23], as well as the percentile method. Each time series consists of 247 months, which can be viewed as a concatenation of 2 separate but uniformly spaced time series—the first containing 181 observations from 05/2002 to 05/2017and the second containing 66 observations from July 2018 to December 2023—with an 11-month gap between them (see Section 3). Given that the stationary bootstrap method assumes uniform data spacing, the distributions and SDs for the estimators of relevant variables were examined by applying the bootstrap only to the initial series of 181 observations. In all cases, the distribution of the estimator was approximately normal, and then the corresponding 95% CI can be calculated as the estimate of the quantity of interest (computed using the complete series of 247 observations) plus or minus 2 SD (estimated from the bootstrap). For notational simplicity, most of the results are presented as "estimate $\pm$ SD". The approach to implementing the stationary bootstrap in this study closely mirrors that employed in the research in [18,19], where more details are provided. For the correlation between the annual/winter/autumn average of the non-seasonal signals of WT components and climate indices in Section 3.4, the reported SDs were obtained using the ordinary bootstrap after testing the null hypothesis that the relevant time series are realizations of independent and identically distributed random variables. To this aim, the test based on the sample autocorrelation function, the turning point test, the difference-sign test, and the rank test were used [24]. In all cases, the number of bootstrap iterations was established at 10,000.

For validation purposes, the analysis was rerun, incorporating an extra cosine term into Equation (2) to accommodate the 161-day signal attributed to S2 aliasing in the GRACE dataset; that is, the aliasing of the semidiurnal solar tide. The outcome of the analyses, both with and without this supplemental cosine term, turned out to be indistinguishable.

2.2. Data

The continental catchment regions draining to the Arabian Gulf were identified according to the global continental runoff pathway scheme, which is a 0.5-degree regular grid [4].

Monthly P and E data were obtained from the ERA5 reanalysis [25,26]. This is a system managed by the European Centre for Medium-Range Weather Forecasts (ECMWF) that combines real-world observations into general atmospheric circulation models. The dataset covers both land and sea. Original data are 0.25-degree regular grids, but they were resampled to a 0.5° regular grid by simple averaging to match the spatial resolution of the continental drainage basin data. The period covered is from 2002 to 2023.

The GRACE and GRACE Follow-On missions measure gravity anomalies with respect to a dynamic geophysical model that accounts for solid and ocean tides, among other factors. Assuming that such gravity anomalies are produced by mass changes on the Earth's surface, such as in the oceans, they can be interpreted as W anomalies [27]. Time variations of W (that is, dW) can be estimated as the discrete central derivative of W. In general, and unless otherwise stated, GRACE and GRACE Follow-On will be referred to simply as GRACE. Among the various existing GRACE products, we used the RL06 GRACE mascon (mass concentration) v2 solution provided by the Center of Space Research (CSR) at the University of Texas at Austin [28–30]. Data were monthly, and the time period was from 05/2002 to 12/2023, with a shortfall of 11 months between 06/2017and 06/2018. In addition, there were cases of missing data for 12 single months and 5 consecutive 2-month periods, which were dealt with by linear interpolation. Then, the studied period was 05/2002–05/2017 and 07/2018–12/2023. Data were in regular 0.25-degree grids, but

as with P and E data, the grids were averaged to 0.5-degree grids to match the spatial resolution of the continental drainage basin data. The obtained spatial resolution was still finer than the ~300 km (~3° near the Equator) resolution of GRACE.

The following standard corrections were applied to these GRACE and GRACE Follow-On data: (1) The C_{20} coefficient was replaced with a solution derived from Satellite Laser Ranging [31], and (2) for GRACE Follow-On data, the C_{30} coefficient was also replaced. (3) As the mission was not sensitive to geo-center variations, an estimate of degree-1 Stokes coefficients was added from modeled water-mass variations [32,33]. (4) Adjustments for glacial isostatic adjustment (GIA) were performed following [34]. In addition to these, we made further adjustments: (5) The bottom pressure product (GAD), responsible for capturing non-tidal variations in both atmospheric and oceanic conditions, was reintroduced into the GRACE data. The ocean's mean value was set to zero to ensure consistency with subsequent correction. (6) The GRACE mission, after correcting for atmospheric mass variations and some ocean dynamics, assumes that the total mass of the system (denoted by the degree-0 Stokes coefficient, ΔC_{00}) is constant. However, this was not true because of the global exchange of water between the Earth's surface and the atmosphere. To correct this imbalance, the ΔC_{00} term from ERA5 P–E was added to dW from GRACE (see [18,19] for further details). Errors in the estimate of the ΔC_{00} term propagated to dW, but they did not affect the estimates of R and N from Equations (1) and (2), respectively, since the ΔC_{00} term vanished due to the residual estimate between dW and $P-E$.

Volume transport was calculated by multiplying the $P-E$ values, expressed in mm/month, by the surface area of a grid cell, which was given in m^2. Conversely, the units for W in the GRACE data were kg/m^2, and for dW, units were (kg/m^2)/month. As such, dW yielded mass transport when it was multiplied by the surface area of a grid cell, also given in m^2. In order to make dW and $P-E$ comparable, the units of dW were converted to volume transport units assuming a water density of 1000 kg/m^3 for freshwater and 1025 kg/m^3 for ocean water. Subsequently, all outcomes will be presented in terms of volume transport and will be denoted in km^3/year.

3. Results

The time series of all the water transport (WT) components in Equations (1) and (2) are depicted in Figure 2. These WT components were estimated according to the regions shown in Figure 1, except when they were compared with the results from Campos et al. (2020) [35]. In this case, the regions were slightly modified (see Supplementary Figure S1) to adjust better to the section at 26°N, defined in Campos et al. (2020) [35], to report the inflows/outflows to/from the Arabian Gulf.

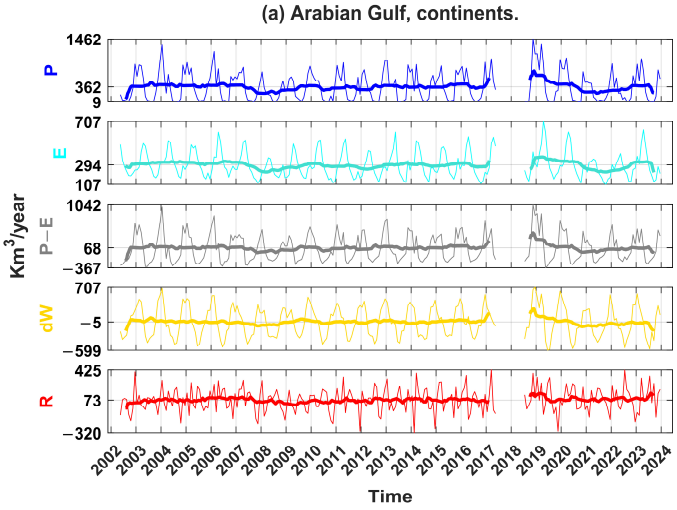

Figure 2. *Cont.*

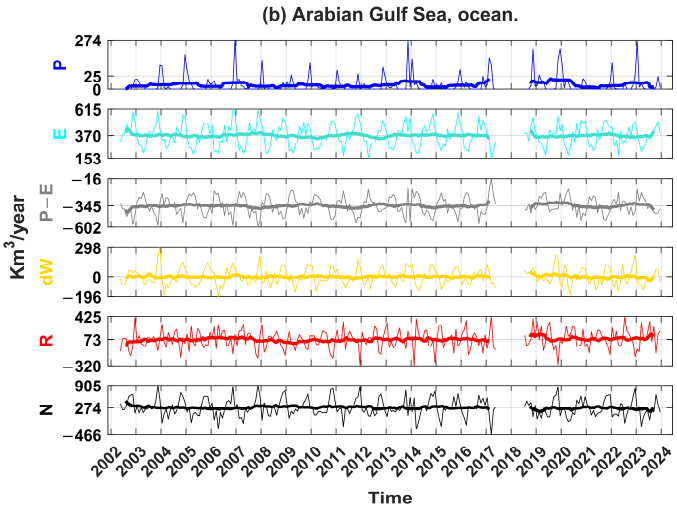

Figure 2. WT time series in the Arabian Gulf for both (**a**) continental drainage basins and (**b**) ocean basins. P is precipitation, E is evaporation, dW is water budget variations, R is the water flux from land to the sea, and N is the net water exchange between the Arabian Gulf and the Indian Ocean through the Strait of Hormuz. Negative (positive) values of N correspond to Arabian Gulf outflows (inflow). Thick lines depict the 12-month moving average. The labels in the y-axis of each time series correspond to their mean, maximum, and minimum values.

3.1. Mean Values

On annual averages, the hydrological cycle of the region is as follows: The continental drainage basins receive 362 ± 14 km^3/year via P and lose 294 ± 5 km^3/year via E. This results in an excess of water that is not stored in the continent (dW is statistically indistinguishable from zero) and is discharged to the sea, causing a R = 73 ± 7 km^3/year. In the Arabian Gulf, the situation is exactly the opposite, as evaporation (E = 370 ± 3 km^3/year) is much higher than precipitation (P = 25 ± 3 km^3/year), resulting in a water deficit of 345 ± 4 km^3/year. Since the water budget in the Arabian Gulf does not change (dW is again statically indistinguishable from zero), the deficit created by net evaporation must be replenished. The contribution from the continents barely covers 25% of this deficit, so 274 ± 10 km^3/year must be imported from the Indian Ocean through the Gulf of Oman. This means that three-quarters of the freshwater deficit in the gulf is covered by saltwater, resulting in high salt concentrations. All mean values are summarized in Table 1, and a schematic representation of the mean water cycle in the Arabian Gulf can be seen in Figure 3.

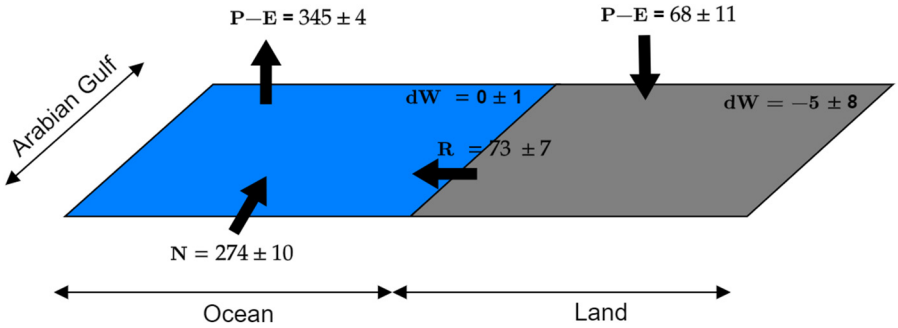

Figure 3. Schematic representation of the mean water cycle in the Arabian Gulf shown in Table 1. Units in km^3/year. Reported values are mean values, based on the original time series (with 247 observations) plus/minus the standard deviation estimated by stationary bootstrap based on the reduced series (with 181 observations).

Table 1. Mean, annual, and semi-annual signals of water transport components in Figure 2, estimated from Equation (3). Units are km^3/year for mean values and amplitudes, and degrees for phases. In each cell, the following are reported: (i) the point estimate (based on the original time series) plus/minus the standard deviation (SD; estimated by bootstrap based on the reduced series; that is, from 181 observations), and (ii) the 95% confidence interval (CI), computed as the point estimate plus/minus 1.96 SD.

		Mean ± SD, km^3/year	Annual Amplitude ± SD, km^3/year	Annual Phase ± SD, Degrees	Semi-Annual Amplitude ± SD, km^3/year	Semi-Annual Phase ± SD, Degrees	Annual Peak
Arabian Gulf drainage basins (1.1421×10^6 km^2)	*P*	362 ± 14 (336, 389)	375 ± 20 (336, 414)	28 ± 3 (23, 34)	26 ± 16 (−5, 57)	100 ± 40 (22, 178)	28 January
	E	294 ± 5 (284, 305)	143 ± 6 (130, 155)	103 ± 3 (98, 109)	57 ± 5 (47, 67)	62 ± 5 (52, 72)	14 April
	P–E	68 ± 11 (46, 89)	365 ± 15 (334, 395)	6 ± 2 (2, 11)	40 ± 14 (12, 68)	38 ± 24 (−8, 85)	6 January
	dW	−5 ± 8 (−21, 10)	396 ± 16 (365, 427)	1 ± 2 (−4, 5)	26 ± 13 (1, 51)	65 ± 25 (17, 114)	1 January
	R	73 ± 7 (59, 88)	48 ± 11 (26, 69)	135 ± 15 (105, 164)	65 ± 13 (39, 91)	49 ± 11 (28, 70)	17 May
Arabian Gulf Sea (2.5112×10^5 km^2)	*P*	25 ± 3 (20, 30)	36 ± 4 (29, 44)	5 ± 6 (−8, 17)	16 ± 4 (8, 23)	165 ± 17 (132, 197)	5 January
	E	370 ± 3 (364, 377)	120 ± 5 (110, 129)	289 ± 2 (284, 293)	49 ± 5 (39, 58)	140 ± 5 (130, 151)	20 October
	P–E	−345 ± 4 (−353, −337)	116 ± 6 (105, 128)	91 ± 3 (86, 96)	35 ± 6 (23, 46)	129 ± 8 (113, 146)	2 April
	dW	0 ± 1 (−2, 3)	82 ± 6 (71, 93)	310 ± 4 (303, 317)	22 ± 5 (13, 31)	114 ± 14 (87, 141)	10 November
	N	274 ± 10 (255, 293)	230 ± 15 (200, 259)	292 ± 4 (285, 299)	95 ± 17 (63, 127)	84 ± 9 (65, 102)	23 October

3.2. Annual Climatology

The WT produced by the different flows does not occur uniformly throughout the year but shows a marked seasonal variation. For each WT component, such an annual climatology is estimated in two ways: (1) an average year is estimated by averaging the signal of all Januarys, all Februarys, and so on (Figure 4), and (2) fitting a linear trend as well as an annual and semi-annual components model, as described in Section 2. Annual and semi-annual amplitudes and phases are reported, with their corresponding SD, in Table 1.

In the continental drainage basin of the Arabian Gulf, the annual cycle variability of $P-E$ mimics that of P, showing a high Pearson correlation between the two original time series (0.93 ± 0.01; Figure 5a), which means that net precipitation is mainly driven by precipitation. Both signals show a range of annual variability around ~719 km^3/year, which is nearly twice that of evaporation (~351 km^3/year). Throughout the year, E is higher than P in spring and summer, and lower in autumn and winter. P reaches its annual maximum (minimum) in January (August) with a value of 748 ± 55 km^3/year (29 ± 2 km^3/year), while E reaches its annual maximum (minimum) in April (September) with a value of 507 ± 21 km^3/year (156 ± 5 km^3/year). This net precipitation pattern reflects a wet season during the winter months and a dry season during the summer months. The evaporation pattern shows higher values during the warmer months of the year, consistent with higher temperatures. The annual cycle of $P-E$ shows a period of net precipitation during the wet season, with a maximum of 489 ± 48 km^3/year in January, and a period of net evaporation during the dry season, with a minimum of −270 ± 9 km^3/year in June. This annual variability modifies the continental water budget and drives the annual variability of dW, whose original time series shows a high Pearson correlation with $P-E$ of 0.89 ± 0.01.

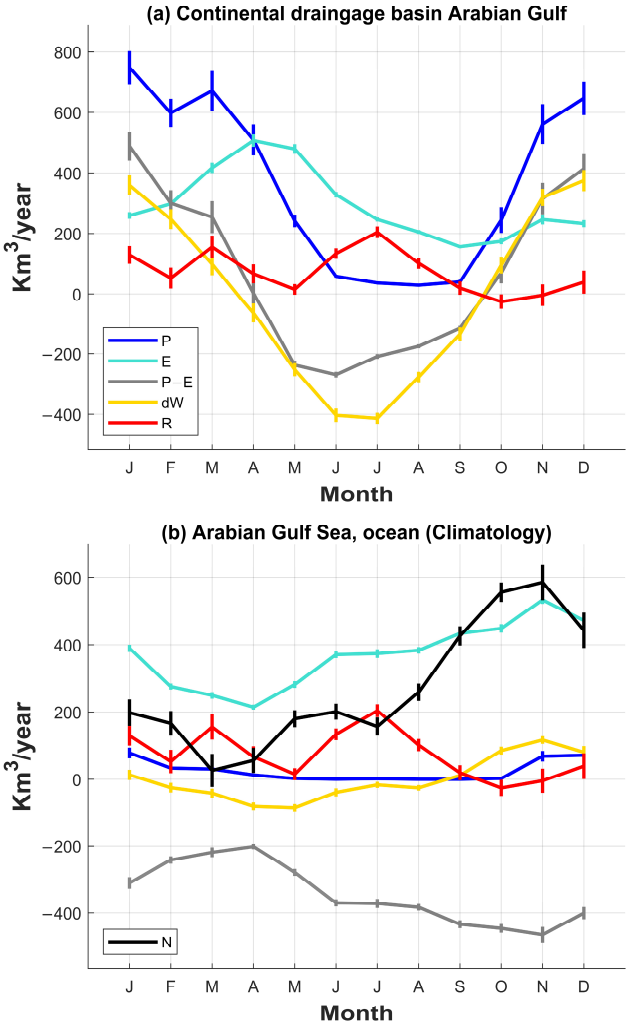

Figure 4. Annual climatology (monthly averages) of signals shown in Figure 2. The error bar of each month is 1 standard deviation of the mean. (**a**) Continental drainage basin and (**b**) Arabian Gulf Sea.

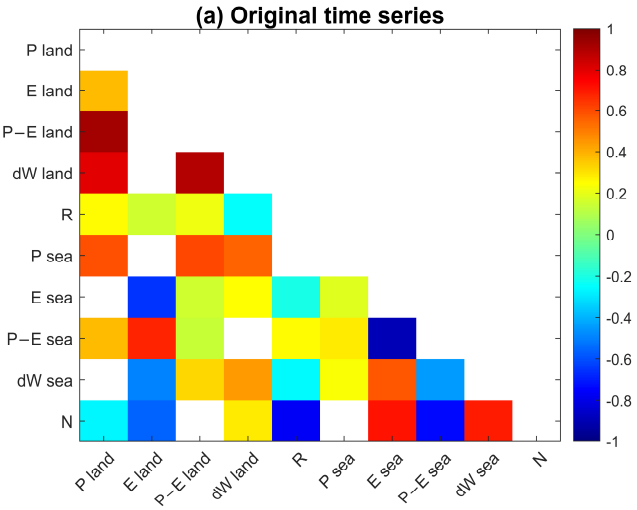

Figure 5. *Cont.*

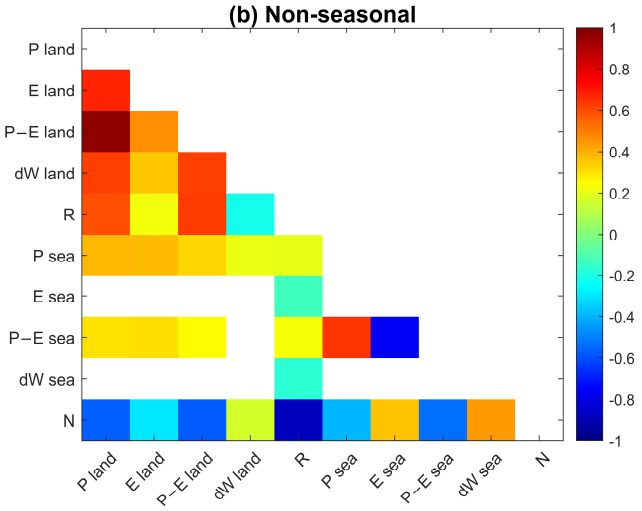

Figure 5. Pearson correlation coefficients between (**a**) the seasonal signals in Figure 2 and (**b**) the non-seasonal signals in Figure 6. White squares represent correlations that are not statistically significant at the 0.05 significance level.

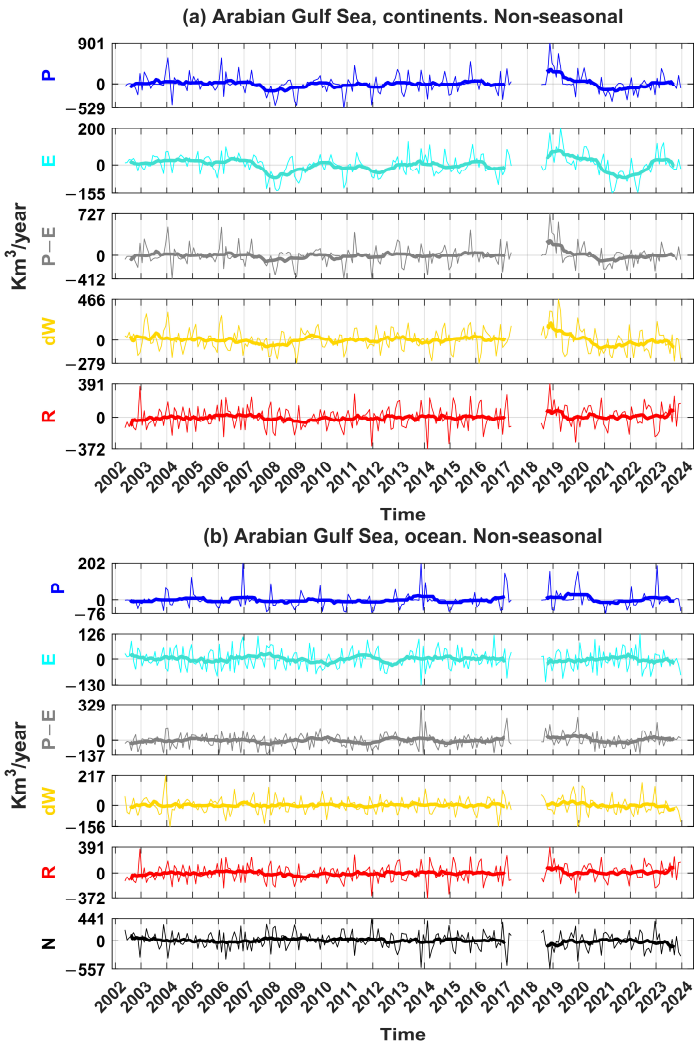

Figure 6. Non-seasonal signal of WT components displayed in Figure 2. The y-axis labels for each time series represent their mean, maximum, and minimum values.

The lowest range of annual variability is observed in R, of about 229 km^3/year. From all annual cycles, R is the furthest from a sinusoidal shape. Even so, it has an annual maximum in the summer months, with a peak of 204 ± 19 km^3/year in July. This evacuation of water into the sea increases, in absolute terms, the minima values of dW in summer (–403 ± 22 km^3/year in June and –414 ± 18 km^3/year in July) to such an extent that the loss of water budget in July is evenly produced between $P-E$ (–210 ± 8 km^3/year) and R. In December, dW reaches an annual maximum of 374 ± 35 km^3/year. The minima values of R are reached in October (–25 ± 24 km^3/year) and November (–4 ± 36 km^3/year). The relationship between R and dW is driven by infiltration and runoff generation mechanisms. Understanding such relationship is critical to developing effective water management strategies. Note that the mean values are negative, but not significantly different from zero. Negative values of R would have no physical meaning. We will return to these values in the Discussion Section.

In the Arabian Gulf, the mean value and annual range of P are only 7% and 18%, respectively, of the continental P. This represents a dramatic reduction. The annual maximum is reached in December and January, with values around 10% of continental P, while the minimum is reached from May to October, when P is absent in the sea. In contrast, the mean E is higher at sea than on land, with a similar annual range of 319 km^3/year. The annual cycle at sea is opposite to that of the continent, reaching a minimum in April (215 ± 7 km^3/year) and a maximum in November (533 ± 12 km^3/year). The original time series of E for land and sea show a high negative correlation, –0.66 ± 0.03.

The large values of E relative to P result in net evaporation during all months of the year. The intra-annual variation of $P-E$ is mainly produced by E, as indicated by the high correlation (–0.89 ± 0.01, Figure 5a) between the original time series. Contrary to what might appear to be the case, dW follows a reverse annual cycle to that of $P-E$. Net evaporation is lowest in April (–202 ± 8 km^3/year), but dW reaches its second largest value in absolute value (among the negative values) that month (–80 ± 12 km^3/year, and –85 ± 11 km^3/year in May). On the other hand, the highest $P-E$ water loss occurs in November (–465 ± 23 km^3/year), when the increase in water mass budget peaks (117 ± 11 km^3/year). This opposite behavior is reflected in the negative correlation of the original series of dW and $P-E$ (-0.45 ± 0.04), and the positive one between dW and E (0.57 ± 0.04). This is possible thanks to the inflow of water from the continent, but above all thanks to the inflow of water from the Indian Ocean through the Strait of Hormuz. The original time series of dW and N display a high positive correlation of 0.69± 0.03, which means that the deficit of water produced by E (and then $P-E$) is overcompensated by N, which ultimately drives the intra-annual variability of dW. It is important to note that the original series of R and N have a high negative correlation, -0.77 ± 0.03. This means that when there is a large contribution from R, N is reduced, as in March, when R = 155 ± 37 km^3/year and N is statistically null. When the contribution of R is minimal (statistically zero), the contribution of N increases, as it happens in October (556± 29 km^3/year) and November (586 ± 53 km^3/year), where N reaches its annual maximum values. This situation is similar to the mean net WT from the Atlantic to the Mediterranean Sea through the Strait of Gibraltar [19]. In contrast to the Strait of Gibraltar net WT, which changes the sign in two months (April and May), here, N always has the same sense. Note, however, that in some specific months, there was a net WT from the Arabian Gulf to the Indian Ocean. For example, in April 2006 $N = -301$ km^3/year, in March 2014 $N = -308$ km^3/year, and in March 2017 $N = -466$ km^3/year.

In summary, P in the Arabian Gulf is higher in the winter months, while E is higher in the late summer and autumn months. The $P-E$ values are negative throughout the year, indicating that E consistently exceeds P. The water budget increases the most in the autumn months and decreases the most in the spring. The Indian Ocean transports water to the Arabian Gulf every month of the year, with maximum transport in autumn.

3.3. Non-Seasonal Signal of WT

The non-seasonal signals (Figure 6) are derived by subtracting the annual climatology (Figure 4) from the original signals (Figure 2). This approach is more appropriate than subtracting an approximation based on annual and semi-annual sinusoids, as in Equation (3), because the annual mean signal is not always close to a sinusoidal shape (see, for example, *R* in Figure 4). In general, all components show a larger non-seasonal variability on land than in the ocean.

In the continental catchment region, the non-seasonal variability of *P* propagates to *P*–*E*, *dW*, and *R*. The Pearson correlation coefficients between *P* and *P*–*E*, *R*, and *dW* are 0.97 ± 0.01, 0.59 ± 0.04, and 0.62 ± 0.05, respectively (Figure 5b). *P* also shows a high correlation with *E* (0.68 ± 0.04), which could be due to the fact that above (below) average amounts of *P* allow for more (less) water to evaporate. Although the correlations between *E* and *P*–*E*, *R*, and *dW* are significant, they are lower than those with *P*, suggesting that *P* is the main driver of non-seasonal variability on land. It is also noteworthy that the correlation between *R* and *P*–*E* increases to 0.63 ± 0.04 when the seasonality is removed.

In general, the annual averages of *P* are close to the mean of the whole period, except for three years: 06/2007–05/2008, 06/2018–05/2019, and 2021 (Figure 6a). In 06/2007–05/2008, *P* presented a below-average value of 153 km^3/year, which produced the following below-average values: *E* = 53 km^3/year, *P*–*E* = 101 km^3/year, and *dW* = 82 km^3/year. No anomalous data were observed in *R*, which means that the below-average *P* was compensated by water stored in the continent. A similar situation occurred in 2021, when a below-average value of *P*= 149 km^3/year resulted in below-average values in the other components (*E* = 68 km^3/year, *P*–*E* = 81 km^3/year, and *dW* = 63 km^3/year), except for *R*. In the period 06/2018–05/2019, the situation was different for two reasons. On the one hand, *P* presented an above-average anomaly of 283 km^3/year, which also increased the other mean values: *E* = 71 km^3/year, *P*–*E* = 212 km^3/year, and *dW* = 164 km^3/year. On the other hand, the anomaly also affected *R*, which had an above-average value of 48 km^3/year.

In the sea, the situation is quite different. For example, although *P* is highly correlated with *P*–*E* (0.64 ± 0.07), it is not significantly correlated with *E* or *dW*. This makes sense because *E* in the sea does not depend on the availability of water at non-geological time scales, which is largely dependent on *P* on land. Also unlike on land, in the sea, *E* is highly correlated with *P*–*E* (–0.77 ± 0.04). Then, non-seasonal *P*–*E* is driven equally by *P* and *E*. For *R* and *N*, the lack of seasonality does not reduce the correlation between them, but slightly increases it up to –0.88 ± 0.02. On the other hand, the correlation between *P*–*E* and *N* decreases slightly up to –0.53 ± 0.06. This means that the loss of water caused by *P*–*E* in the sea is not replaced by *R*, but it is mainly compensated by water from the Indian Ocean, on both seasonal and non-seasonal scales (Figure 7).

In the sea, the interannual variability of the WT components shows less variability than that observed in the continent. The most notable anomaly occurred during the period 06/2018–05/2019, when an above-average *P* (14 km^3/year) and below-average *E* (13 km^3/year) resulted in an above-average *P*–*E* (27 km^3/year). This, combined with an above-average *R* (48 km^3/year), reduced the Indian Ocean input to 57 km^3/year. The following section will delve deeper into the relationship between WT components and the primary interannual signals.

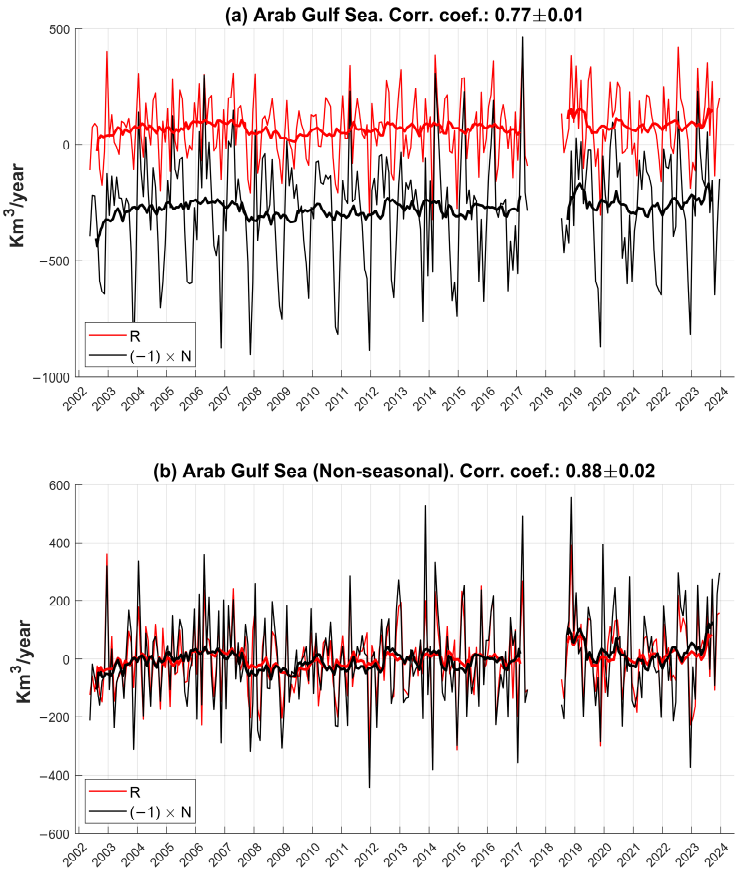

Figure 7. (**a**) Seasonal and (**b**) non-seasonal water transport from land to the Arabian Gulf (red curve) and net inflow to the Arabian Gulf (black curve). Black curve represents $-N$. As N is multiplied by -1, positive (negative) values of the black curve represent above-average (below-average) flows. Correlations between R and N are negative in both cases.

3.4. Climatic Teleconnections

The North Atlantic Oscillation (NAO) is a climate phenomenon characterized by fluctuations in the atmospheric pressure difference between the Icelandic Low and the Azores High, two semi-permanent pressure systems situated in the North Atlantic. The NAO affects climatic variables, such as temperature, precipitation, and wind patterns, across the North Atlantic and adjacent continental regions. Its influence even reaches into and around the Arabian Gulf. As seen in Section 3.2, most of the annual precipitation is produced during the winter months of December to March. This is because the subtropical jet moves southwards in winter, bringing extratropical storms to the region. The latter are more (less) common and intense during the positive (negative) NAO phase, which results in stronger (weaker) moisture flux entering the region and more (less) precipitation, especially between 30°N and 40°N latitudes [36]. The correlation between the annual average of the non-seasonal signal of P over land and the NAO index (downloaded from [37]) is 0.55 ± 0.23. Since the non-seasonal signal of P is correlated with R and dW, there is also a correlation of annual NAO with annual R and dW of 0.51 ± 0.21 and 0.47 ± 0.26, respectively. In the ocean, annual P is also significantly correlated with annual NAO (0.46 ± 0.2). Kumar et al. [38] found the opposite relationship between the NAO index and P over the Arabian Peninsula; that is, that negative (positive) NAO is associated with above-normal (below-normal) P. However, this finding does not contradict our results, as most of the continental catchment of the Arabian Gulf lies between 30°N and 40°N latitudes, and only a small portion is on the Arabian Peninsula.

El Niño-Southern Oscillation (ENSO) is a cyclical climate pattern characterized by changes in the winds and sea surface temperatures (SST) in the tropical Pacific Ocean.

The positive (negative) phase of ENSO, known as El Niño (La Niña), is characterized by a weakening or reversal (strengthening) of the easterly winds, which displaces warm surface waters into the central and eastern (western) Pacific. Among the different methods of characterizing the ENSO phases, we chose the Oceanic Niño Index downloaded from [39], which measures the sea surface temperature (SST) anomalies in the Niño 3.4 region (5°N–5°S, 170°W–120°W). It is well known that positive ONI values are related to positive ENSO phases. The ENSO modifies *P* patterns around the globe [40,41]. In the Arabian Gulf and the surrounding continental area, El Niño events modify winter patterns and moisture transport, increasing the winter *P* [42–44]. On land, we found a positive correlation between non-seasonal winter (mean of December, January, February, and March) *P* land and ONI of 0.46 ± 0.19, and between winter *E* land and ONI of 0.52 ± 0.15. Additionally, we observed a negative correlation between the winter ONI and *E* sea of -0.44 ± 0.17. Besides, there were significant correlations between the ONI and the autumn means of continental *E* (0.69 ± 0.11), *P*–*E* (0.63 ± 0.12), *dW* (0.5 ± 0.21), and *P* (0.68 ± 0.12). In the Arabian Gulf, the correlations with ONI were lower (*P*, 0.43 ± 0.15) or statistically insignificant.

The Indian Ocean Dipole (IOD) is a coupled ocean–atmosphere phenomenon, similar to ENSO, that is responsible for the SST gradient between the eastern and western equatorial Indian Ocean. The positive phase of the IOD modifies the Walker circulation over the tropical Indian Ocean and, hence, the moisture transport, resulting in, among other impacts, an increase in autumn *P* in coastal East Africa [45], a strengthening of the summer Indian monsoon [46], and a decrease in *P* in Australia [47]. Although the positive phase of the IOD increases in autumn and early winter in southern Iran [48], the Arabian Gulf and its continental catchment region are not among the most impacted IOD regions. The Indian Ocean Dipole Mode Index (DMI, downloaded from [49]) is used to quantify the phases of the IOD. The Pearson correlation coefficients between DMI and our WT components were weak or nonexistent. However, if we take the autumn averages (September, October, November, and December), significant correlations between the DMI and continental *P* (0.46 ± 0.14), *E* (0.49 ± 0.16), and *P*–*E* (0.42 ± 0.15) were observed. Similarly, significant correlations were observed between the DMI and oceanic *P* (0.51 ± 0.2) and *P*–*E* (0.49 ± 0.19).

Figure 8 shows a summary of all the correlations between the WT components and the NAO, ENSO, and IOD. These three climate indices are not independent (uncorrelated) events, and the relationship between them may be complicated. For example, the IOD is neither completely independent of ENSO, since half of the IOD events are understood to be an extension of ENSO, nor completely related, since the other half of the IOD events are independent of ENSO [50,51]. On the other hand, the NAO is also connected to the IOD [52], and the relationship between NAO and ENSO is highly complex [53,54]. A more detailed study of WT interannual variability is left for a follow-up study.

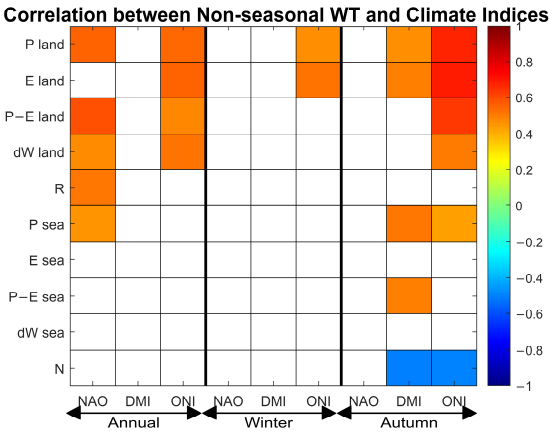

Figure 8. Pearson correlation coefficients between the WT components of the region and the NAO, ENSO, and IOD climate indices. Correlations are estimated for annual, winter, and autumn means. White squares represent correlations that are not statistically significant at the 0.05 significance level.

4. Discussion

In this study, we used GRACE and ERA5 data to investigate the hydrological cycle of the Arabian Gulf and its surrounding continental catchment region. The methodology employed has previously been successfully applied in the main ocean basins [18], the Mediterranean and Black Seas [19], and the Baltic Sea [20]. However, the Arabian Gulf is of a smaller size, approaching the resolution limit of this method, which is constrained by the ~300 km spatial resolution of GRACE. This limitation mainly arises from those grid points situated in proximity to the coastline, where signal leakage resulting from topographic effects becomes a significant concern. This is the reason why the grid points in the continental catchment region that are closer than 111 km to the coast (2 grid points in the resampled regular grid) were deleted. For example, if those points were not eliminated, the climatology of R would have significantly negative values in October (–107 $\pm$ 25 km^3/year) and November (–63 $\pm$ 45 km^3/year). Those months with negative R represent a WT from sea to land, which could be explained by the transport of desalinated water from the sea to the continents. However, although the Arabian Gulf countries produce about 45% of the global desalinated water, it accounts for only 4 km^3/year [3], which is insufficient to explain the negative values of R. Another potential explanation for these negative values could be the infiltration of seawater into the continental underground water deposits, although there are currently no measurements to support this hypothesis. It is our contention that these negative values are an artifact, produced by a leakage signal from the sea in continental points near the coast in GRACE measurements.

The results obtained here were analyzed on an average, seasonal, and non-seasonal scale. In general, we found good agreement with previous results. For example, our climatology of P for the continental catchment was similar to that obtained for the Arabian Peninsula in [55], despite some differences in the study area and time period.

Chao et al. [56] reported two climatologies of E from the literature with annual minima of ~180 km^3/year in April and May, and maxima of ~700 km^3/year in November and December, which are consistent with our results. They developed a numerical model driven by those values of E, plus the addition of climatological winds and net ocean heat gain. Their model showed an inflow from the Gulf of Oman of 3784 km^3/year that was offset by an equal outflow. The model assumed a null net WT though the Strait of Hormuz. However, subsequent in situ measurements showed that this was not the case. Between 12/1996 and 03/1998, the GOGP99 experiment collected hydrographic and moored acoustic Doppler current profiler data, among others, near the Strait of Hormuz. Johns et al. [11] estimated a net inflow of 631 $\pm$ 1625 km^3/year. This was the result of a shallow inflow in the northern part of the Strait of Hormuz of 7253 $\pm$ 1161 km^3/year, and two outflows in the southern part: a shallow one of 1892 $\pm$ 631 km^3/year, and a deep one of 4730 $\pm$ 946 km^3/year. This net inflow is twice our estimate. Nevertheless, a study carried out by Pous et al. [9], a year later, using the same data, showed that the net inflow was very sensitive to the reference level and the average velocity assumed for the calculation of geostrophic currents. Depending on the assumptions, they reported a net inflow of 1261 km^3/year, which is twice as much as the value reported by Johns et al. [11], and another net inflow of 315 km^3/year, which is similar to our annual estimate. In any case, the data used by Pous et al. [9] covered 10-11/1999, and in these months, we observed the largest net flux, with values of 559 km^3/year and 594 km^3/year, respectively. We note that the comparison for a given year is complex by year-to-year variations. For example, in 10-11/2010, we reported a net flow of 765/803 km^3/year, while in 2018, we found 448/106 km^3/year.

In more recent years, numerical models have been able to estimate the net WT transport as a residual between inflows and outflows. Hassanzadeh et al. [2] estimated a net inflow into the Arabian Gulf of 946 km^3/year using a 3D numerical model based on momentum, volume, heat, and salt conservation. Xue and Elthahir [57] developed a coupled ocean–atmosphere model for the region, named GARM (Gulf–Atmosphere Regional Model). Among others, the model uses two atmospheric model outputs to set initial and boundary conditions: ECHAM5 and ERA40. The simulated climatology of the WT in the Arabian Gulf

for the period 1981–1990 is shown in Figure 9. Regardless of the expected discrepancies due to differences in methodology, data, and time period, the mean values and climatologies were generally in good agreement. Mean values for the simulation with ECHAM5 (those from ERA40 were similar) showed the following values in km^3/year: P = 19, E = 433, R = 49, inflow = 7919, outflow = 7554, and N = 365 (positive, so net inflow). The climatologies of P and E were more similar to our results than those of R and N. The R derived from the model showed a more sinusoidal climatology with a single peak in April, unlike our estimate, which showed three local maxima in January, March, and July. For N, both estimates showed lower values at the beginning of the year and higher values in summer and autumn. Although the differences in summer were clear, our estimate was much smaller than that of the model. In a more recent study, Campos et al. [35] applied the HYCOM numerical model to study the WT through the Strait of Hormuz. The model was forced by surface air temperature, radiation fluxes, precipitation, vapor mixing ratio, and winds from the NCEP-1 reanalysis product, and showed a net inflow through a section at a latitude of 26°N (see Figure 1) of 385 km^3/year. Two years later, Campos et al. [58] published a net inflow through the same section of 435 $\pm$ 126 km^3/year following a similar methodology but including ocean tides and rivers. If we estimate N at the same section as Campos et al. [58] (Supplementary Figure S1), we obtain 280 km^3/year. This value is slightly higher than that reported in Table 1. In general, all N values reported in the literature were higher than those reported in our study. Table 2 lists these values, and their mean (excluding the values of Pous et al. [9], which showed excessive variability, and Chao et al. [56], which assumed null net flow) was 517 $\pm$ 122 km^3/year.

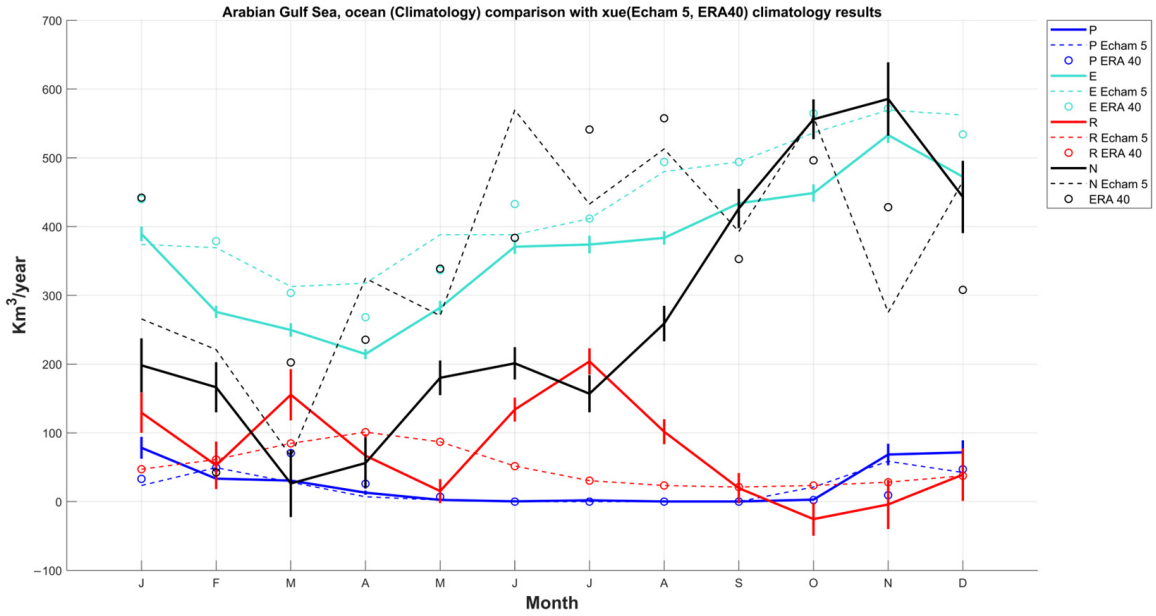

Figure 9. Monthly climatology of water transport components in the Arabian Gulf from this study (solid thick lines) and Xue et al. (2015) [57]. The dashed lines (circles) are estimates using atmospheric data from ECHAM5 (and ERA40 data).

The approach presented in this study has its strengths and drawbacks. On the one hand, our method was not able to calculate horizontal inflows and outflows of seawater, as other models do. On the other hand, previous models usually use statistical values for R, while our method made an estimate for each month. Both analyses could be integrated if, for example, the model fed in our values of R and used our estimate of N as a constraint. This could improve the performance of the model by producing more realistic input and output flows, or at least be compatible with more types of data, such as GRACE. In this sense, this study not only adds new information to the understanding of the dynamics

of the Strait of Hormuz, but also serves as a unique tool to recalibrate and reinterpret previous research.

Table 2. Net water transport (N) between the Arabian Sea and the Arabian Gulf, as estimated by previous studies. Positive (negative) values of N indicate water inflow into (outflow from) the Arabian Gulf.

	Specifications	Period	Mean $N \pm$ SD, km^3/year
Chao, 1992 [56]	Numerical model.	First 400 days	0
Johns et al., 2003 [11]	Combination of hydrographic and ADCP data.	12/1996–03/1998	631
Pous et al., 2004 [9]	ADCP measurement: each derives from different assumptions.	10–11/1999	1216; 315; 3784
Hassanzadeh et al., 2012 [2]	Theoretical model.	Not specified	946
Xue and Eltahir, 2015 [57]	Coupled ocean–atmosphere GARM model. Atmospheric boundary: ECHAM5/ERA-40.	1981–1990	365/360
Campos et al., 2020 [35]	HYCOM numerical model. No rivers, no tides.	1980–2015	385
Campos et al., 2022 [58]	HYCOM numerical model. Rivers, tides.	01/2002–12/2006	435 $\pm$ 126
Literature summary	Mean $\pm$ SD of these values (excluding this study, Chao 1992 [56], and the highest value of Pous et al., 2004 [9]).		517 $\pm$ 122
This study	GRACE and ERA5 atmospheric model.	05/2002–05/2017 and 07/2018–12/2023	274 $\pm$ 10

In addition to studying the averages of the hydrological cycle in the Arabian Gulf over the last two decades, we also studied seasonal and non-seasonal variations. Seasonal variations were very pronounced for all WT components and should be taken into account when planning in situ measurement campaigns. On the other hand, interannual variations were influenced by several climatic indices. This multifactorial dependence complicates the understanding of the interannual variability and should be addressed in future work.

Finally, the description of the average hydrological cycle over the last two decades provides a benchmark for future comparisons. This will be important for measuring future variations in the hydrological cycle that are expected to occur as a result of the ongoing accelerated climate change. The study of seasonal and non-seasonal variations has also contributed to a better understanding of the dynamics of WT in the region. As mentioned above, the interannual variability is influenced by several climatic indices. In particular, the influence of the NAO, in combination with other large-scale climate indices, such as ENSO and IOD, plays a crucial role in the regional hydro-climatology, emphasizing the teleconnections of remote regions and their local manifestations. This multifactorial dependence adds further complexity to our understanding of the interannual variability of WT.

Supplementary Materials: The following supporting information can be downloaded at: https://www.mdpi.com/article/10.3390/rs16193577/s1. Figure S1: Region used to estimate the net inflow of seawater (N) for comparison with the results of Campos et al. (2020; 2022) [35,58]. The difference with Figure 1 is in the Strait of Hormuz.

Author Contributions: Conceptualization, A.K.B.; methodology, D.G.-G. and A.K.B.; software, A.K.B.; validation, D.G.-G., J.-M.S., A.K.B. and M.I.V.; formal analysis, M.T. and M.I.V.; investigation, A.K.B., D.G.-G. and J.-M.S.; data curation, A.K.B.; writing—original draft preparation, A.K.B.; writing—review and editing, D.G.-G., A.K.B., J.-M.S., M.T. and M.I.V.; visualization, A.K.B.; supervision, D.G.-G.; funding acquisition, M.I.V. All authors have read and agreed to the published version of the manuscript.

Funding: This research was supported by grant PID2021-122142OB-I00 funded by MCIN/AEI/10.13039/501100011033, grant PROMETEO/2021/030 funded by Generalitat Valenciana, and grants GVA-THINKINAZUL/2021/035 and GVA-THINKINAZUL/2021/043 funded by Generalitat Valenciana and "European Union NextGenerationEU/PRTR". A.K.B. benefits from a doctoral study allowance financed by the Algerian Ministry of Higher Education and Scientific Research.

Data Availability Statement: Publicly available datasets were analyzed in this study. These data can be found at the following links. Copernicus Climate Data Store: https://cds.climate.copernicus.eu/cdsapp#!/home. Center for Space Research at the University of Texas: https://www2.csr.utexas.edu/grace/. NOAA Climate Prediction Center North Atlantic Oscillation (NAO) Index: https://www.cpc.ncep.noaa.gov/products/precip/CWlink/pna/nao.shtml. NOAA Physical Sciences Laboratory ENSO Data: https://psl.noaa.gov/enso/data.html. NOAA Physical Sciences Laboratory DMI Data: https://psl.noaa.gov/gcos_wgsp/Timeseries/Data/dmi.had.long.data.

Acknowledgments: All data used in this study are publicly available, and we thank all the organizations that provided them. ERA5 data were provided by the Copernicus Climate Change Service Climate Data Store (CDS): https://cds.climate.copernicus.eu/cdsapp#!/home (accessed on 11 June 2024). GRACE time-variable gravity data were provided by CSR, University of Texas: http://www2.csr.utexas.edu/grace (accessed on 11 June 2024). North Atlantic Oscillation (NAO) data were from the NOAA Climate Prediction Center (CPC): https://www.cpc.ncep.noaa.gov/products/precip/CWlink/pna/nao.shtml (accessed on 11 June 2024). ENSO data were from the NOAA Physical Sciences Laboratory: https://psl.noaa.gov/enso/data.html (accessed on 11 June 2024). DMI data were from the NOAA Physical Sciences Laboratory: https://psl.noaa.gov/gcos_wgsp/Timeseries/Data/dmi.had.long.data (accessed on 11 June 2024).

Conflicts of Interest: The authors declare no conflicts of interest. The funders had no role in the design of the study; in the collection, analyses, or interpretation of data; in the writing of the manuscript, or in the decision to publish the results.

References

1. Vasou, P.; Vervatis, V.; Krokos, G.; Hoteit, I.; Sofianos, S. Variability of water exchanges through the Strait of Hormuz. *Ocean Dyn.* **2020**, *70*, 1053–1065. [CrossRef]
2. Hassanzadeh, S.; Hosseini Balam, F.; Rezaei-Latifi, A. Three–dimensional numerical modeling of the water exchange between the Persian Gulf and the Gulf of Oman through the Strait of Hormuz. *Oceanol. Hydrobiol. Stud.* **2012**, *41*, 85–98. [CrossRef]
3. Lattemann, S.; Höpner, T. Environmental impact and impact assessment of seawater desalination. *Desalination* **2008**, *220*, 1–15. [CrossRef]
4. Oki, T.; Sud, Y.C. Design of Total Runoff Integrating Pathways (TRIP)-A Global River Channel Network. *Earth Interact.* **1998**, *2*, 1–37. [CrossRef]
5. Sultan, S.A.R.; Elghribi, N.M. Temperature Inversion in the Arabian Gulf and the Gulf of Oman. *Cont. Shelf Res.* **1996**, *16*, 1521–1544. [CrossRef]
6. Durgadoo, J.V.; Rühs, S.; Biastoch, A.; Böning, C.W.B. Indian Ocean Sources of Agulhas Leakage. *J. Geophys. Res. Oceans* **2017**, *122*, 3481–3499. [CrossRef]
7. Sheehan, P.M.F.; Webber, B.G.M.; Sanchez-Franks, A.; Matthews, A.J.; Heywood, K.J.; Vinayachandran, P.N. Injection of Oxygenated Persian Gulf Water into the Southern Bay of Bengal. *Geophys. Res. Lett.* **2020**, *47*, e2020GL087773. [CrossRef]
8. Ghazi, E.; Bidokhti, A.A.; Ezam, M.; Azad, M.T.; Hassanzadeh, S. Physical Properties of Persian Gulf Outflow Thermohaline Intrusion in the Oman Sea. *Open J. Mar. Sci.* **2017**, *7*, 169–190. [CrossRef]
9. Pous, S.P.; Carton, X.; Lazure, P. Hydrology and Circulation in the Strait of Hormuz and the Gulf of Oman—Results from the GOGP99 Experiment: 1. Strait of Hormuz. *J. Geophys. Res.* **2004**, *109*, C12037. [CrossRef]
10. L'Hégaret, P.; de Marez, C.; Morvan, M.; Meunier, T.; Carton, X. Spreading and Vertical Structure of the Persian Gulf and Red Sea Outflows in the Northwestern Indian Ocean. *J. Geophys. Res. Oceans* **2021**, *126*, e2019JC015983. [CrossRef]
11. Johns, W.E.; Yao, F.; Olson, D.B.; Josey, S.A.; Grist, J.P.; Smeed, D.A. Observations of seasonal exchange through the Straits of Hormuz and the inferred heat and freshwater budgets of the Persian Gulf. *J. Geophys. Res.* **2003**, *108*, 3391. [CrossRef]
12. Held, I.M.; Soden, B.J. Robust Responses of the Hydrological Cycle to Global Warming. *J. Clim.* **2006**, *19*, 5686–5699. [CrossRef]
13. Huntington, T.G. Evidence for Intensification of the Global Water Cycle: Review and Synthesis. *J. Hydrol.* **2006**, *319*, 83–95. [CrossRef]
14. Greve, P.; Orlowsky, B.; Mueller, B.; Sheffield, J.; Reichstein, M.; Seneviratne, S.I. Global Assessment of Trends in Wetting and Drying Over Land. *Nat. Geosci.* **2014**, *7*, 716–721. [CrossRef]
15. Durack, P.J.; Wijffels, S.E.; Matear, R.J. Ocean Salinities Reveal Strong Global Water Cycle Intensification During 1950 to 2000. *Science* **2012**, *336*, 455–458. [CrossRef] [PubMed]
16. Markonis, Y.; Papalexiou, S.M.; Martinkova, M.; Hanel, M. Assessment of Water Cycle Intensification Over Land Using a Multisource Global Gridded Precipitation Dataset. *J. Geophys. Res. Atmos.* **2019**, *124*, 11175–11187. [CrossRef]
17. IPCC. Summary for Policymakers. In *Climate Change 2023: Synthesis Report; Contribution of Working Groups I, II and III to the Sixth Assessment Report of the Intergovernmental Panel on Climate Change*; Core Writing Team, Lee, H., Romero, J., Eds.; IPCC: Geneva, Switzerland, 2023; pp. 1–34. [CrossRef]
18. García-García, D.; Vigo, M.I.; Trottini, M. Water transport among the world's ocean basins within the water cycle. *Earth Syst. Dynam.* **2020**, *11*, 1089–1106. [CrossRef]

19. García-García, D.; Vigo, M.I.; Trottini, M.; Vargas, J.; Sayol, J.M. Hydrological cycle of the Mediterranean-Black Sea system. *Clim. Dyn.* **2022**, *59*, 1919–1938. [CrossRef]
20. Boulahia, A.K.; García-García, D.; Vigo, M.I.; Trottini, M.; Sayol, J.-M. The Water Cycle of the Baltic Sea Region From GRACE/GRACE-FO Missions and ERA5 Data. *Front. Earth Sci.* **2022**, *10*, 879148. [CrossRef]
21. Ma, N.; Zhang, Y.; Szilagyi, J. Water-Balance-Based Evapotranspiration for 56 Large River Basins: A Benchmarking Dataset for Global Terrestrial Evapotranspiration Modeling. *J. Hydrol.* **2024**, *630*, 130607. [CrossRef]
22. Politis, D.N.; Romano, J.P. The Stationary Bootstrap. *J. Am. Stat. Assoc.* **1994**, *89*, 1303–1313. [CrossRef]
23. Patton, A.; Politis, D.N.; White, H. Correction to "Automatic Block Length Selection for the Dependent Bootstrap". *Economet. Rev.* **2009**, *28*, 372–375. [CrossRef]
24. Brockwell, P.J.; Davis, R.A. *Introduction to Time Series and Forecasting*, 2nd ed.; Springer: New York, NY, USA, 2010.
25. Hersbach, H.; de Rosnay, P.; Bell, B.; Schepers, D.; Simmons, A.; Soci, C.; Abdalla, S.; Alonso-Balmaseda, M.; Balsamo, G.; Bechtolg, P.; et al. *Operational Global Re-Analysis: Progress, Future Directions, and Synergies with NWP*; ERA Report Series 27; European Centre for Medium Range Weather Forecasts: Berkshire, UK, 2018.
26. Copernicus Climate Change Service (C3S). ERA5: Fifth Generation of ECMWF Atmospheric Reanalyses of the Global Climate. Available online: https://cds.climate.copernicus.eu/cdsapp#!/dataset/reanalysis-era5-single-levels-monthly-means?tab=form (accessed on 11 June 2024).
27. Chao, B.F. Caveats on the Equivalent Water Thickness and Surface Mascon Solutions Derived from the GRACE Satellite-Observed Time-Variable Gravity. *J. Geod.* **2016**, *90*, 807–813. [CrossRef]
28. Save, H. CSR GRACE RL06 Mascon Solutions. In *Texas Data Repository Dataverse*; Texas Digital Library: Austin, TX, USA, 2019. [CrossRef]
29. Save, H.; Bettadpur, S.; Tapley, B.D. High Resolution CSR GRACE RL05 Mascons. *J. Geophys. Res.-Solid* **2016**, *121*, 7547–7569. [CrossRef]
30. Center for Space Research, University of Texas at Austin. GRACE/GRACE-FO. Available online: https://www2.csr.utexas.edu/grace/ (accessed on 11 June 2024).
31. Cheng, M.; Ries, J. The unexpected signal in GRACE estimates of C20. *J. Geod.* **2017**, *91*, 897–914. [CrossRef]
32. Swenson, S.; Chambers, D.; Wahr, J. Estimating Geocenter Variations from a Combination of GRACE and Ocean Model Output. *J. Geophys. Res.* **2008**, *113*, B08410. [CrossRef]
33. Sun, Y.; Riva, R.; Ditmar, P. Optimizing Estimates of Annual Variations and Trends in Geocenter Motion and J2 From a Combination of GRACE Data and Geophysical Models. *J. Geophys. Res. Solid Earth* **2016**, *121*, 8352–8370. [CrossRef]
34. Peltier, W.R.; Argus, D.F.; Drummond, R. Comment on "An Assessment of the ICE-6GC (VM5a) Glacial Isostatic Adjustment Model" by Purcell et al. *J. Geophys. Res.-Solid* **2018**, *123*, 2019–2028. [CrossRef]
35. Campos, E.J.D.; Gordon, A.L.; Kjerfve, B.; Vieira, F.; Cavalcante, G. Freshwater budget in the Persian (Arabian) Gulf and exchanges at the Strait of Hormuz. *PLoS ONE* **2020**, *15*, e0233090. [CrossRef]
36. Hunt, K.M.R.; Zaz, S.N. Linking the North Atlantic Oscillation to winter precipitation over the Western Himalaya through disturbances of the subtropical jet. *Clim. Dyn.* **2023**, *60*, 2389–2403. [CrossRef]
37. Climate Prediction Center, National Weather Service, NOAA. North Atlantic Oscillation (NAO). Available online: https://www.cpc.ncep.noaa.gov/products/precip/CWlink/pna/nao.shtml (accessed on 11 June 2024).
38. Kumar, K.N.; Abouelmagd, A.; McCabe, M.F.; Molini, A. Precipitation over the Arabian Peninsula: Global Forcing and Teleconnections. In Proceedings of the European Geosciences Union (EGU) General Assembly, Vienna, Austria, 27 April–2 May 2014. [CrossRef]
39. NOAA Physical Sciences Laboratory. Oceanic Niño Index (ONI). Available online: https://psl.noaa.gov/enso/data.html (accessed on 11 June 2024).
40. Ropelewski, C.F.; Halpert, M.S. Global and Regional Scale Precipitation Patterns Associated with the El Niño/Southern Oscillation. *Mon. Wea. Rev.* **1987**, *115*, 1606–1626. [CrossRef]
41. Dai, A.; Wigley, T.M.L. Global Patterns of ENSO-Induced Precipitation. *Geophys. Res. Lett.* **2000**, *27*, 1283–1286. [CrossRef]
42. Niranjan Kumar, K.; Ouarda, T.B.M.J. Precipitation Variability Over UAE and Global SST Teleconnections. *J. Geophys. Res. Atmos.* **2014**, *119*, 10313–10322. [CrossRef]
43. Niranjan Kumar, K.; Ouarda, T.B.M.J.; Sandeep, S.; Ajayamohan, R.S. Wintertime Precipitation Variability Over the Arabian Peninsula and Its Relationship with ENSO in the CAM4 Simulations. *Clim. Dyn.* **2016**, *47*, 2443–2454. [CrossRef]
44. Sandeep, S.; Ajayamohan, R.S. Modulation of Winter Precipitation Dynamics Over the Arabian Gulf by ENSO. *J. Geophys. Res. Atmos.* **2018**, *123*, 198–210. [CrossRef]
45. Black, E.; Slingo, J.; Sperber, K.R. An Observational Study of the Relationship Between Excessively Strong Short Rains in Coastal East Africa and Indian Ocean SST. *Mon. Wea. Rev.* **2003**, *131*, 74–94. [CrossRef]
46. Ashok, K.; Guan, Z.; Yamagata, T. Impact of the Indian Ocean dipole on the relationship between the Indian monsoon rainfall and ENSO. *Geophys. Res. Lett.* **2001**, *28*, 4499–4502. [CrossRef]
47. Ashok, K.; Guan, Z.; Yamagata, T. Influence of the Indian Ocean Dipole on the Australian Winter Rainfall. *Geophys. Res. Lett.* **2003**, *30*, 1821. [CrossRef]
48. Pourasghar, F.; Tozuka, T.; Jahanbakhsh, S.; Sari Sarraf, B.; Ghaemi, H.; Yamagata, T. The Interannual Precipitation Variability in the Southern Part of Iran as Linked to Large-Scale Climate Modes. *Clim. Dyn.* **2012**, *39*, 2329–2341. [CrossRef]

49. NOAA Physical Sciences Laboratory. Indian Ocean Dipole Mode Index (DMI). Available online: https://psl.noaa.gov/gcos_wgsp/Timeseries/Data/dmi.had.long.data (accessed on 11 June 2024).
50. Meyers, G.; McIntosh, P.; Pigot, L.; Pook, M. The Years of El Niño, La Niña and Interactions with the Tropical Indian Ocean. *J. Clim.* **2007**, *20*, 2872–2880. [CrossRef]
51. Vinayachandran, P.N.; Francis, P.A.; Rao, S.A. Indian Ocean Dipole: Processes and Impacts. *Curr. Trends Sci.* **2009**, *46*, 569–589.
52. Jiang, J.; Liu, Y. Impact of March North Atlantic Oscillation on Indian Ocean Dipole: Role of Air–Sea Interaction Over the Western North Pacific. *Clim. Dyn.* **2023**, *61*, 1089–1104. [CrossRef]
53. Brönnimann, S. Impact of El Niño–Southern Oscillation on European Climate. *Rev. Geophys.* **2007**, *45*, RG3003. [CrossRef]
54. Zhang, W.; Wang, Z.; Stuecker, M.F.; Turner, A.G.; Jin, F.F.; Geng, X. Impact of ENSO Longitudinal Position on Teleconnections to the NAO. *Clim. Dyn.* **2019**, *52*, 257–274. [CrossRef]
55. Niranjan Kumar, K.; Entekhabi, D.; Molini, A. Hydrological Extremes in Hyperarid Regions: A Diagnostic Characterization of Intense Precipitation Over the Central Arabian Peninsula. *J. Geophys. Res. Atmos.* **2015**, *120*, 1637–1650. [CrossRef]
56. Chao, S.-Y.; Kao, T.W.; Al-Hajri, K.R. A numerical investigation of circulation in the Arabian Gulf. *J. Geophys. Res.* **1992**, *97*, 11219–11236. [CrossRef]
57. Xue, P.; Eltahir, E.A.B. Estimation of the Heat and Water Budgets of the Persian (Arabian) Gulf Using a Regional Climate Model. *J. Clim.* **2015**, *28*, 5041–5062. [CrossRef]
58. Campos, E.J.D.; Kjerfve, B.; Cavalcante, G.; Vieira, F.; Abouleish, M. Water exchange across the Strait of Hormuz. Effects of tides and rivers runoff. *Reg. Stud. Mar. Sci.* **2022**, *52*, 102336. [CrossRef]